# A Fluorescent Probe for Protein Misfolding and Aggregation Due to Oxidative Stress Based on a 7-Azaindole-BODIPY Derivative

Diego Herrera-Ochoa,[a] Iván Llano,[b] Consuelo Ripoll,[a] Pierre Cybulski,[c] Martin Kreuzer,[d] Susana Rocha,[c,*] Eva M. García-Frutos,[b,e,*] Iván Bravo,[a] and Andrés Garzón-Ruiz[a.*]

[a] *Departamento de Química Física, Facultad de Farmacia, Universidad de Castilla-La Mancha, Av. Dr. José María Sánchez Ibáñez, s/n, 02071 Albacete, Spain.*

[b] *Instituto de Ciencia de Materiales de Madrid (ICMM), CSIC, Cantoblanco, 28049 Madrid, Spain.*

[c] *Molecular Imaging and Photonics, Department of Chemistry, KU Leuven, Leuven Chem&Tech, Celestijnenlaan 200F, 3001, Leuven, Belgium*

[d] *ALBA Synchrotron Light Source, Carrer de la Llum 2-26, Cerdanyola del Valles, 08290 Cerdanyola Del Vallès, Barcelona, Spain*

[e] *Departamento de Química Orgánica y Química Inorgánica, Facultad de Ciencias, Universidad de Alcalá, Campus Científico Tecnológico, Av. de Madrid, 28802, Alcalá de Henares, Madrid, Spain*

## ABSTRACT

The development of new fluorescent probes as molecular sensors is a critical step for the understanding of molecular mechanisms. Probes based on BODIPY offer remarkable versatility in molecular sensing due to their unique properties. BODIPY-based probes exhibit high fluorescence quantum yields, exceptional photostability, and tunable absorption/emission wavelengths. Here, we report the synthesis and evaluation of a novel 7-azaindole-BODIPY derivative to probe hydrophobic proteins as well as protein misfolding and aggregation. In organic solvents, this compound exhibits two emissive excited states efficiently interconverting. In contrast, within aqueous environments, the formation of molecular aggregates induces distinct photophysical properties. The complex photophysics of this 7-azaindole-BODIPY derivate were used as a starting point to explore its sensing applications. In presence of albumin, the monomeric form of the probe is stabilized in the hydrophobic regions of the protein, leading to a significant increase of both the fluorescence emission intensity and lifetime. A similar effect was observed when the probe interacts with protein aggregates. Notably, the fluorescence emission is less sensitive to the presence of other macromolecules such as pepsin, DNA, Ficoll 40, and coconut oil. Fluorescence lifetime imaging microscopy (FLIM) and two-photon fluorescence

microscopy performed on breast cancer cells (MCF-7) and lung cancer cells (A549) incubated with this probe revealed longer fluorescence lifetimes and higher emission intensity upon oxidative stress. It is known that cellular stress leads to the accumulation and aggregation of misfolded proteins. Protein misfolding in MCF-7 cells under oxidative stress conditions was confirmed by synchrotron FTIR microspectroscopy. These results show that protein misfolding and aggregation triggered by oxidative stress can be monitored using the probe here developed.

**KEYWORDS:** azaindole-BODIPY, hydrophobic proteins, protein aggregation, cellular stress probe, FLIM, Two-photon fluorescence microscopy, synchrotron FTIR microspectroscopy

## INTRODUCTION

The combination of boron dipyrromethene (BODIPY) and indole has been widely explored to develop fluorescent probes for biological applications.[1–3] On the one hand, BODIPY is a well-known fluorescent dye and its derivatives are universally used in fluorescence imaging.[1–3] On the other hand, indole is an electron-rich aromatic heterocyclic organic compound used for sensing a wide range of analytes, particularly anions.[4–7] Despite the promising results reported for indole-BODIPY derivatives in fluorescence sensing applications, the combination of azaindole and BODIPY has received less attention. Azaindole is an aromatic heterocycle consisting of pyridine ring fused to a pyrrole ring and, hence, electron-richer than indole. Many azaindoles exhibit biological activity and pharmacological properties including antitumor activity.[8] Nevertheless, only three azaindole-BODIPY derivatives have been characterized to date (compounds **2** – **4** in Figure 1).[9,10] Compound **2** has showed a good performance as ratiometric probe for the detection of $F^-$ ions in human colorectal carcinoma cells (HCT 116) by Mahapatra et al.[9] Later, the sensitivity to $HSO_4^-$ of compounds **3** and **4** was studied by Keşan et al.[10]

Here, we present the synthesis of a novel 7-azaindole-BODIPY derivative (compound **1**), the study of its photophysical properties and the evaluation of its use as a fluorescent probe for hydrophobic proteins as well as protein misfolding and aggregation associated with oxidative stress. It is well known

that the oxidative stress leads to accumulation and aggregation of misfolded proteins in cells due to diverse processes such as modification of chaperone protein activity, amino acid carboxylation, cysteine oxidation, among others.[11,12] The oxidative stress and protein aggregation are involved in biological aging and diverse diseases.[11,13,14] In the present work, we demonstrate that the photophysical properties of compound **1** are sensitive to hydrophobic proteins as well as the hydrophobicity changes associated with the formation of protein aggregates. The response of compound **1** to cellular stress events was monitored by fluorescence lifetime imaging microscopy (FLIM) and two-photon fluorescence microscopy in different cell lines. Protein structural changes of cells under oxidative stress conditions were studied by synchrotron FTIR microscopy.

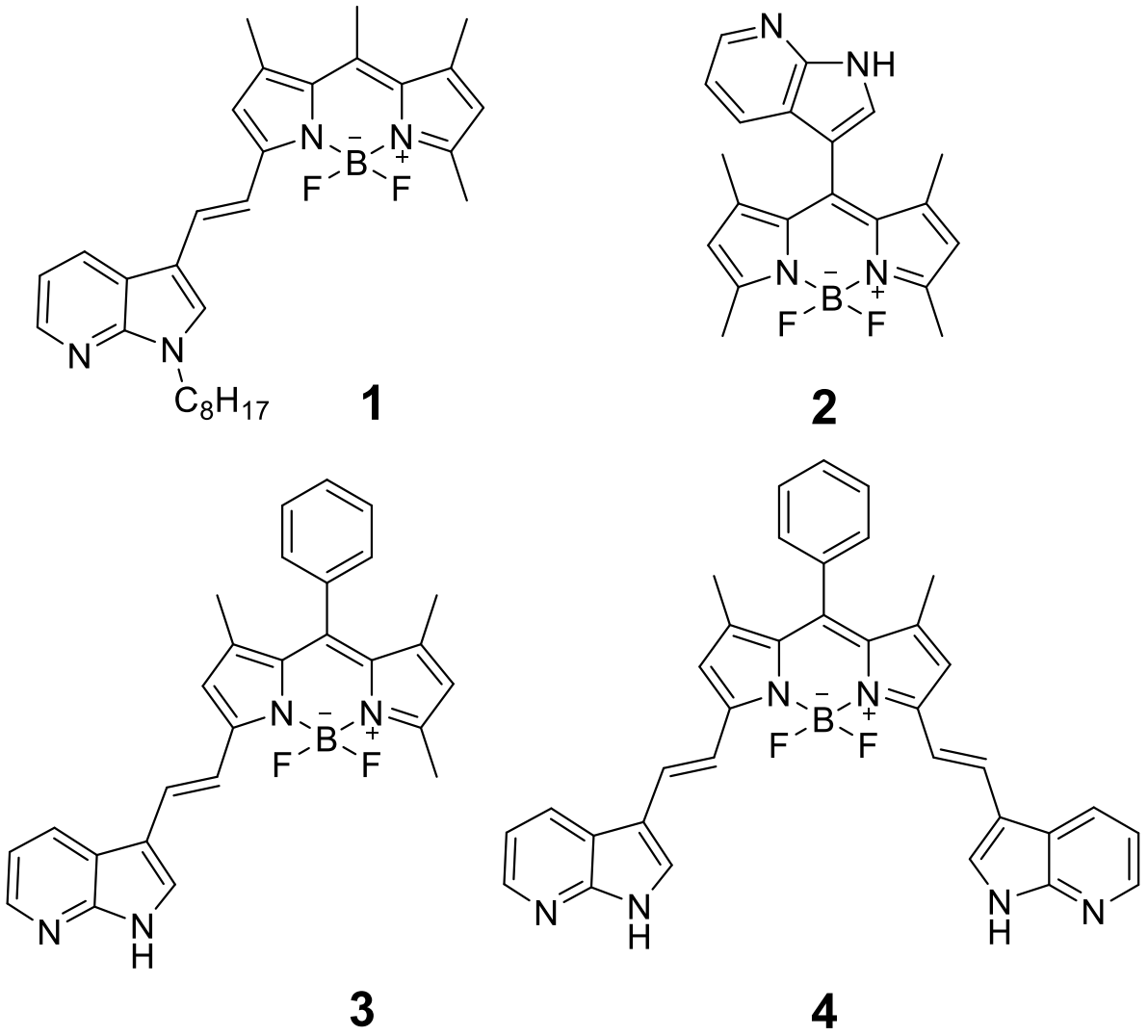


**Figure 1.** Chemical structure of the synthetized compound (**1**) and other reported 7-azaindole-BODIPY derivatives (**2 - 4**)[9,10]

## MATERIALS AND METHODS

**Materials.** All chemicals were commercial and used without further purification. 7-azaindole, toluene, 1-iododoctane, phosphorus (V) oxychloride ($POCl_3$), 5,5-difluoro-1,3,7,9,10-pentamethyl-5H-dipyrrolo[1,2-c:2',1'-f][1,3,2]diazaborinin-4-ium-5-uide (boron dipyrromethene, BODIPY), acetic acid, piperidine and silica gel plates of type 60 F254 with a layer thickness of 0.2 mm were purchased from Sigma Aldrich. Acetone was purchased from VWR International. Tetrabutylammonium hydrogen sulfate [$(Bu)_4N(HSO_4$, phase-transfer catalyst (PTC)] was provided by TCI. Potassium hydroxide (KOH) was acquired from Merk. Hexane, dichloromethane ($CH_2Cl_2$), magnesium sulfate anhydrous ($MgSO_4$) and silica gel 60, 0.04-0.06 mm for flash chromatography and analytical thin layer chromatography (TLC) were purchased from Scharlab. Dimethylformamide (DMF) were provided by Fisher Chemicals and Panreac, respectively. Finally, ultrapure water (Type I, 18.2 MΩ·cm) was used throughout the work. $^1H$ and $^{13}C$ NMR spectra were determined in $CDCl_3$ on a BRUKER AVANCE 300MHz instrument (300.1 and 75.5 MHz for $^1H$ and $^{13}C$, respectively). Chemical shifts (δ) are quoted in parts per million (ppm), referenced to the residual solvent.

**Spectroscopic Characterization Experiments.** UV-Vis absorption spectra were recorded in a V-650 (Jasco) spectrophotometer using a slit width of 0.4 nm and a scan rate of 600 nm $min^{-1}$. A Peltier accessory was employed to control the temperature of the spectrophotometer measuring cell. Steady-state fluorescence spectra were recorded in a FLS920 (Edinburgh Instruments) spectrofluorometer equipped with a 450 W Xe lamp as excitation source, a MCP-PMT (microchannel plate-photomultiplier tube) detector (R3809 model) and a TCSPC (time-correlated single photon counting) data acquisition card (TCC900 model). A FS5 spectrofluorometer (Edinburgh Instruments) equipped with an integrating sphere, a 150 W Xe lamp as the light source and a PMT (photomultiplier tube) detector (R928P model) was employed to determine fluorescence quantum yields. A TLC 50 temperature-controlled cuvette holder (Quantum Northwest) was used for all the fluorescence experiments. The temperature was fixed at 20ºC.

Time-resolved fluorescence emission was collected in a microscope (PicoQuant) equipped with a TCSPC card and two TAU-SPAD-100 avalanche photodiode detectors. Samples were excited with a 511 and 637 nm diode pulse lasers with a repetition rate of 10 MHz. TCSPC resolution was 16 ps and the emission was recorded using 550/49 and 690/70 bandpass filters. The fluorescence intensity decay, I(t), was fitted to the following multiexponential function using an iterative least-square fit method

$$I(t) = \sum_{i=1}^{n} \alpha_i \exp(-t/\tau_i) \quad (1)$$

where $\alpha_i$ and $\tau_i$ are the amplitude and lifetime for each $i^{th}$ term. The mean lifetime of the decay was then calculated as

$$\tau_m = \frac{\sum_{i=1}^{n} \alpha_i \tau_i^2}{\sum_{i=1}^{n} \alpha_i \tau_i} \quad (2)$$

**Cell Cultures.** For FLIM experiments, human breast cancer MCF-7 cells (ATCC HTB-22) were cultured at 37°C in a 5% $CO_2$ humidified atmosphere, with DMEM (Dulbecco's Modified Eagle Medium) cell culture medium, 10% FBS, 1% penicillin-streptomycin and 1% glutamine. For two-photon fluorescence microscopy experiments, A549 cells (CCL-185) were cultured at 37°C in a 5% $CO_2$ humidified atmosphere, with DMEM cell culture medium, 10% FBS, 1% 1-glutamax and 0.1% gentamicin.

The spheroids culture protocol was based on the study reported by Van Zundert *et al.*[15] Briefly, A549 cells were seed in agarose microtissues previously prepared and were kept at 37°C in a 5% $CO_2$ humidified incubator for 10 days, until the spheroids reached the desired size or morphology. The culture medium was refreshed every 2-3 days. Then, cells were harvested of agarose microtissues and transferred to a 1.5 mL microcentrifuge tube.

**Viability Assays.** The MTT (3-(4,5-dimethylthiazol-2-yl)-2,5-diphenyltetrazolium bromide) assay was performed on MCF-7 cells to assess the cytotoxicity of compound 1. A 96-well plate with 10000 cells/well was cultured in DMEM without phenol red at 37°C in a 5% $CO_2$ humidified atmosphere for 24 hours. Cells were treated with different concentrations of 1, within a range of 25 to 500 nM, for 2 and 24 hours. The MTT assay was carried out according to the producer's instructions using a Multiskan Go plate reader spectrophotometer (Thermo Scientific). The cell viability was calculated based on the absorbance of the treated and untreated cells. The results were expressed as percent

viability, considering the cell viability of the control cells (untreated) as 100%. Three independent measurements were carried out for each sample concentration and exposure time and the results were presented as the average value with ±2σ standard deviation.

**Fluorescence Lifetime Imaging of Cells**. MCF-7 cells were seeded onto 20 mm square glass cover slides into 6-well plates and cultured with DMEM medium without phenol red at 37°C in a 5% $CO_2$ humidified atmosphere until the cells reached 50−80% confluence. Cells were incubated with 0.1 μM of compound **1** in serum-free DMEM medium without phenol red for different times (0.5, 1 and 3 hours). To induce cellular stress, some cells were also incubated with ethanol, hydrogen peroxide or cisplatin, along with **1** for different times (0.5, 1 and 3 hours). Hydrogen peroxide is commonly used to induce oxidative stress.[16–18] MCF-7 cells were exposed to a hydrogen peroxide dose of 0.5 mM, two-fold higher than the maximum concentration used by Mahalingaiah *et al.* to study on the oxidative stress in the same type of cells.[16] A concentration of 10 μM was chosen for cisplatin within the order of magnitude of $IC_{50}$ values reported for MCF-7 cells in previous works.[19–23]

After incubation, the cells were washed five times with PBS. After the treatment, FLIM images of the cells were acquired using a MicroTime 200 microscope (PicoQuant). A diode pulse laser of 511 nm (10 MHz and ~0.9 μW) was chosen as excitation source. TCSPC resolution was 16 ps and the emission was collected using a 690/70 bandpass filter. 80×80 μm regions were scanned with 156 nm/pixel spatial resolution and a dwell time of 2 ms. FLIM images were processed using SymphoTime64 software (PicoQuant). The fluorescence intensity decays of each pixel were fitted to the equation (1) using an iterative least-squares fit method (all the fluorescence decays were best fitted to a three-exponential equation).

Two-photon fluorescence imaging of 2D cell cultures. A549 cells were seed in 29-mm, glass-bottom dishes (Cellvis, Mountain View, CA, USA) and grown until ~70% confluency before adding compound **1**. Cells were incubated with 0.1 μM of **1** in DMEM medium without phenol red for different times (0.5, 1 and 3 hours). To induce cellular stress, cells were incubated with ethanol (1 M) along with 1 for different times (0.5, 1 and 3 hours).

After the treatment, fluorescent images were recorded using a Leica TCS SP8 dive microscope (Leica microsystems) with a multi-photon Insight X3 laser and an HC PL IRAPO 40× water objective (NA 1.1). A two-photon pulse laser excitation of 1022 nm was chosen as excitation source. Scanning speed and the image format were set at 400 Hz and 1024 × 1024 pixels. The emission was recorded in two different wavelength ranges (515 - 575 nm and 650 - 725 nm) using two HyD hybrid detectors.

Two-photon fluorescence imaging of cell spheroids. A549 cell spheroids were cultured as described above and were grown until reached the required size. Then, spheroids were incubated with 0.1 μM of compound **1** in DMEM medium without phenol red for 24 hours. After the treatment, fluorescent images were recorded using a Leica TCS SP8 dive microscope (Leica microsystems) with a multi-photon Insight X3 laser and FLUOTAR VISIR 25× water objective (NA 0.95). Two-photon pulse laser excitation, scanning speed and image format were identical to 2D cell fluorescent imaging described above. The emission was recorded by a HyD hybrid detector between 650 - 725 nm.

**Synchrotron-Based FTIR Microspectroscopy.** The SR-FTIR measurements were conducted at the MIRAS beamline at the ALBA synchrotron, Barcelona (Spain), as the synchrotron light was used as the infrared light source, coupling with the 3000 Hyperion microscope coupled to a Vertex 70v spectrometer and a liquid nitrogen-cooled mercury cadmium telluride (MCT) detector.[24] The spectroscopic data were collected in transmission mode using the 36X Schwarzschild objective and condenser and an aperture size of 10×10 μm.

Two samples of control MCF-7 cells and two samples of MCF-7 cells treated with cisplatin were measured. Cells were seeded onto 13 mm diameter and 0.5 mm thick $CaF_2$ glass into 6-well plates and cultured with DMEM medium at 37°C in a 5% $CO_2$ humidified atmosphere until the cells reached 50−80% confluence. Cells were incubated with 10 μM of cisplatin in serum-free DMEM medium for 3 hours. Cells were fixed with 4% formaldehyde for 15 min at room temperature. A total number of 193 control cells and 194 of cisplatin-treated cells were measured, the average spectra are presented. The data were collected in the 4000–800 $cm^{-1}$ mid-infrared range at a spectral resolution of 4 $cm^{-1}$ with 256 co-added scans per spectrum. The OPUS 8.2 (Bruker, Ettlingen, Germany) software package was used for data acquisition. Rubber-band baseline correction and vector normalization were performed

for each single spectrum. The ratios of absorbances at different wavenumbers and the second derivatives were carried out by using of the Quasar software.[25]

**Computational details.** Full geometry optimizations were performed using the Gaussian16 (revision C.01)[26] suite of programs at the BLYP/6-31G* level of theory[27–29] (including solvent effects). Polarizable Continuum Model (PCM) was employed to include the solvent (water) effect.[30,31] The electronic vertical transitions were calculated at the time-dependent (TD)-BLYP/6-31G* level (including solvent effects). In general, the most popular DFT functionals show a poor performance in the calculation of electronic transitions of BODIPY derivatives.[32,33] Surprisingly, some pure generalized gradient approximation (GGA) functionals as BLYP lead to small deviations between calculated electronic transition wavelengths and absorption maximum wavelengths in BODIPY derivatives.[32]

## RESULTS AND DISCUSSION

**Preparation of Compound 1.** The synthesis pathways for preparation of the 7-azaindole-BODIPY **1** is shown in Scheme 1 and Supporting Information. The incorporation of the alkyl chain from of commercially available 7-azaindole (7AI) was carried out by using 1-iodooctane, KOH, the phase-transfer catalyst (PTC) in acetone at 75ºC for 24 hours to give compound 7AI-5 (65%). Compound 7AI-6 was obtained by Vilsmeier-Haack reaction of 7AI-5 with $POCl_3$ in DMF to yield a yellow oil with 68%. Finally, Knoevenagel reaction method was used for the preparation of the novel 7-azaindole-BODIPY derivative, **1**, by treating of compound 7AI-6 with BODIPY in presence of piperidine, acetic acid in in a Dean-Stark apparatus with toluene for 48 hours. The new 7-azaindole-BODIPY derivative, **1**, was isolated by column chromatography to afford the new monostyryl compound in 5% yield as a pink powder. All compounds were identified through $^{1}H$, $^{13}C$ NMR and mass spectrometry (see Supporting Information).

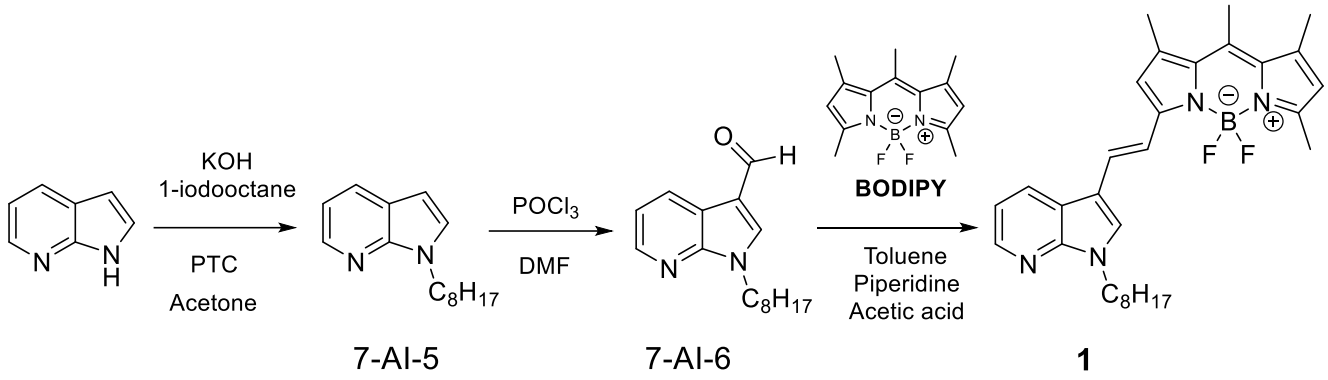


**Scheme 1.** Synthetic route of compound **1**

**Spectroscopic Characterization.** An extended spectroscopic characterization was carried out to evaluate the suitability of compound **1** as a fluorescent probe. The absorption spectrum of **1** in THF shows vibronic structure with an absorption maximum wavelength at 584 nm ($\lambda_{ab}^{max}$) and a shoulder at about 536 nm (Figure 2a and Table S1). Similar vibronic structure was found for **1** in other organic solvents such as toluene, ethanol and DMSO. The structured absorption bands observed in the absorption spectrum of **1** suggests a planar and highly conjugated structure, as confirmed by DFT calculations (Figure 3a). Compound **3**, the previously reported molecule with the most closely related structure, displayed a similar absorption spectrum with a $\lambda_{ab}^{max}$ of 574 nm in acetonitrile solution.[10] Compound **2**, on the other hand, exhibited a significantly blue-shifted absorption maximum ($\lambda_{ab}^{max}$ = 501 nm in an acetonitrile-water mixture)[9] revealing the role of the ethylene bridge in the extension of the electronic conjugation in 7-azaindole-BODIPY system. Additionally, the presence of a second 7-azaindole group leaded to a substantial red-shift of the absorption band of compound **4** ($\lambda_{ab}^{max}$ = 655 nm in acetonitrile solution).[10] TD-DFT calculations revealed that the band centered at 584 nm corresponds to the $S_0 \rightarrow S_1$ transition involving the HOMO and LUMO (Figure 3c and Table S3).

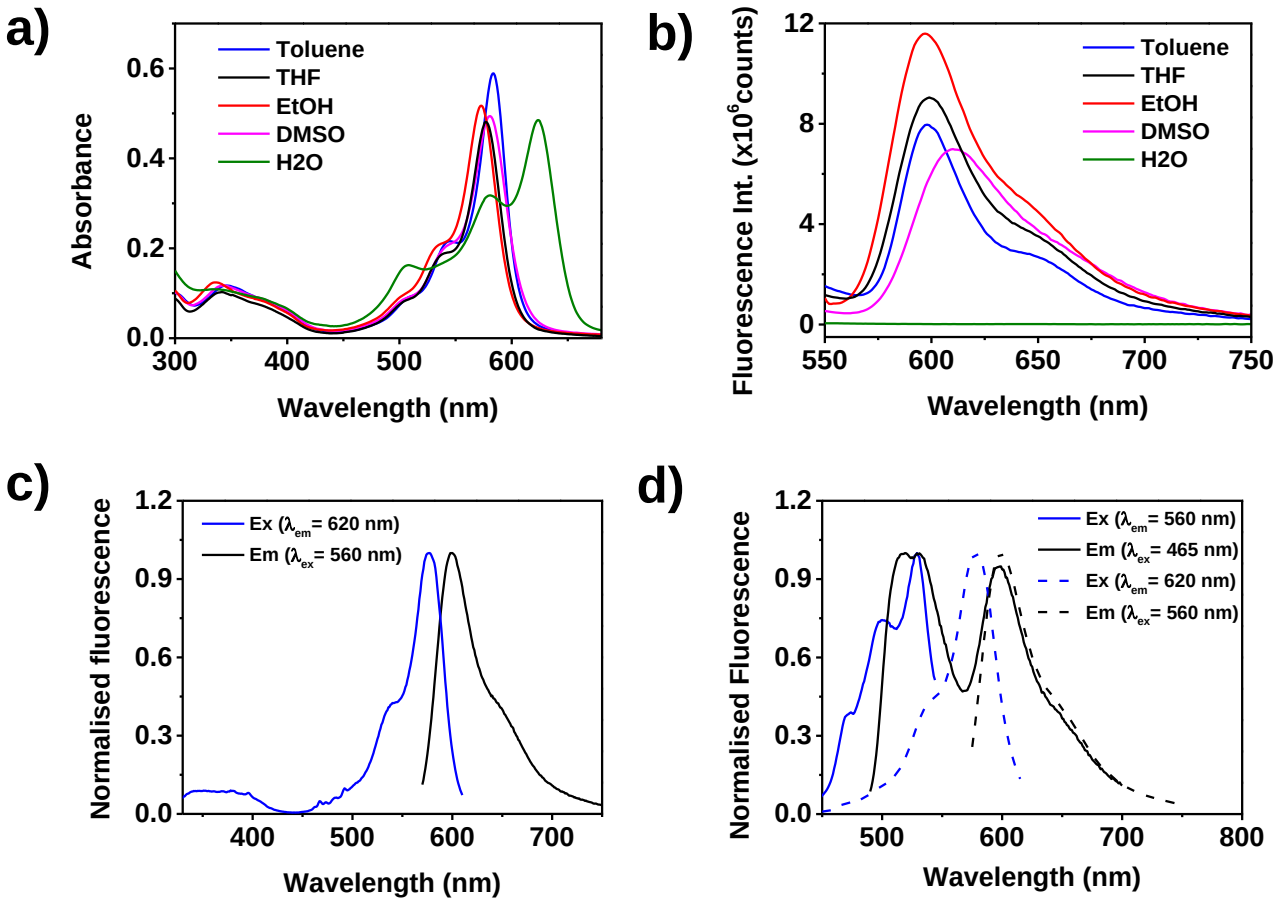


**Figure 2.** Spectroscopic characterization of compound **1**. (a) UV-Vis absorption spectrum in different solvents (sample concentration was 70 µM). (b) Fluorescence emission spectrum in different solvents ($\lambda_{ex}$ = 511 nm; sample concentration was 10 µM). (c) Fluorescence excitation and emission spectra in THF. (d) Different fluorescence excitation and emission bands found in THF solution depending on the experimental conditions.

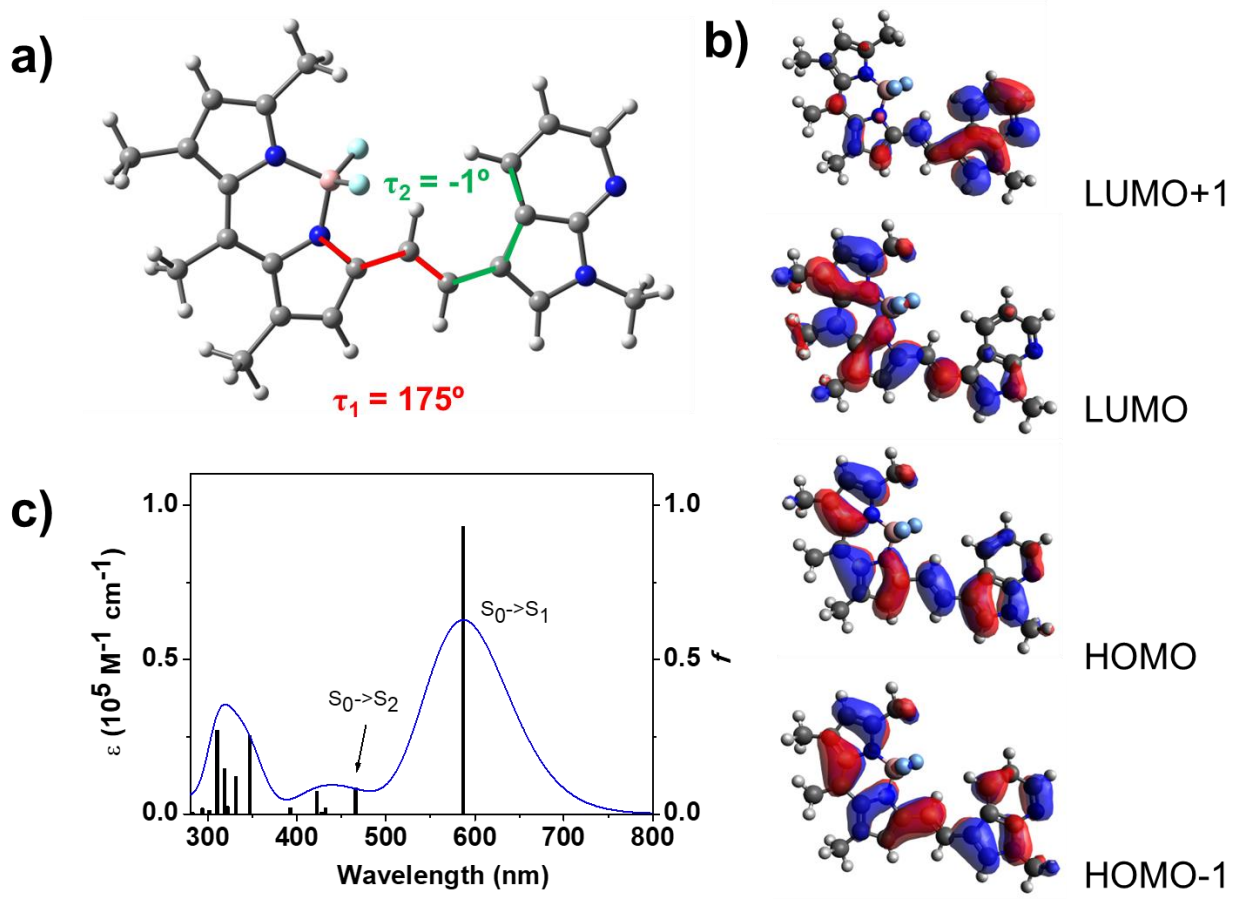


**Figure 3.** Computational study performed for **1** at the BLYP/6-31G* level of theory including CPCM solvation effects (tetrahydrofuran). (a) Molecular structure showing two selected dihedral angles ($\tau_1$ and $\tau_2$). (b) Frontier molecular orbitals. (c) Simulated absorption spectrum. Vertical bars correspond to the oscillator strengths, *f*, calculated for the vertical electronic transitions at the TD-BLYP/6-31G* level of theory (a half-width at half-maxima of 0.20 eV was employed for the simulation of the absorption spectra).

The excitation and emission spectra of **1** follow the mirror rule (Figures 2b, 2c and S2), with excitation and emission maxima ($\lambda_{ex}^{max}$ and $\lambda_{em}^{max}$) in THF at 576 and 598 nm, respectively (see Table S1 for other solvents). When dissolved in DMSO, a red-shift in the emission band was observed ($\lambda_{em}^{max}$ = 611 nm) due to the intramolecular charge-transfer character of the $S_0 \rightarrow S_1$ transition. As shown in Figure 3b, the HOMO is delocalized across the whole molecule while the LUMO is mainly localized within the BODIPY moiety (similar findings were reported for compound **3**).[10] The fluorescence emission decay from the $S_1$ state follows a mono-exponential profile with a lifetime, $\tau_F$, of 3.2 ns and a fluorescence quantum yield, $\Phi_F$, of 58% in THF (Figure S3 and Table S2). These results are consistent with those previously reported for compound **3** ($\tau_F$ = 4.2 ns and $\Phi_F$ = 42% in acetonitrile solution).[10] Furthermore, additional minor excitation bands were detected at shorter wavelengths (around 530 nm and 350 – 400 nm), which were also observed in the absorption spectrum (Figure 2c).

The excitation band observed at approximately 530 nm was attributed to the $S_0 \rightarrow S_2$ transition involving HOMO-1, HOMO, LUMO and LUMO+1. The resolution of this band in the absorption spectrum was hindered by its overlap with the tail of the most intense absorption band (assigned to the $S_0 \rightarrow S_1$ transition). Interestingly, when **1** was excited at 465 nm, two emission bands emerged, centered at 525 and 598 nm. This excitation wavelength avoided the direct excitation of the $S_1$ state but allowed the excitation of the $S_2$ state (Figure 2d and Table S1). Thus, the first emission band (525 nm) corresponds to the fluorescence emission from the $S_2$ state while the second emission band (598 nm) is associated with the emission from the $S_1$ state preceding internal conversion (IC) from the $S_2$ state (hereafter noted as $S_2/S_1 \rightarrow S_0$). Of note, the fluorescence intensity in both emission maxima showed a linear correlation with the fluorophore concentration, ruling out the formation of aggregates (Figure S4). The similar intensity of both emission bands suggests that $S_2/S_1 \rightarrow S_0$ is an efficient IC process that competes against the fluorescence emission from the $S_2$ state. Accordingly, comparable fluorescence lifetimes were found for both processes (4.3 ns for $S_2 \rightarrow S_0$ and 3.9 ns for $S_2/S_1 \rightarrow S_0$; see Table S2). Note that the fluorescence emission decay from the $S_2/S_1 \rightarrow S_0$ process also follows a mono-exponential profile, with a lifetime 0.7 ns longer than for the $S_1 \rightarrow S_0$ process. This increase in the fluorescence lifetime indicates the association with a IC process.

As far as we know, the existence of two emissive states in BODIPY derivatives has been scarcely reported. Cho *et al.* observed that some BODIPY derivatives in THF solution leaded to 'anomalous' emission from the $S_2$ excited state[34] while Schäfer *et at.* have reported the existence of two emissive states in BODIPY dye films.[35] The possible combined use of both emissive states could offer unique advantages in bioimaging applications. It is possible to excite the $S_2$ state using blue light (465 nm) and collect the fluorescence emission in the red spectral range from the $S_1$ state (600 – 750 nm) mediating an IC process. The large difference between the excitation and collection wavelengths reduces the impact of the background fluorescence in microscopy images of biological samples. Noteworthy, red fluorescence emission was observed even when exciting **1** with ultraviolet light (at 350 nm), indicating additional IC processes between high-energy excited states and $S_1$. The presence of the unusual $S_2/S_1 \rightarrow S0$ process prompted the investigation of the sensing potential of compound **1**.

In aqueous solution, a quite different photophysical behavior was observed compared to organic solvents. As shown in Figure 2a, a new and intense absorption band appears at 625 nm while the peak associated to the $S_0 \rightarrow S_1$ transition remains at 580 nm. The new red-shifted band was attributed to the presence of molecular aggregates.[36] Figure 4a shows the effect of the temperature on the stability of aggregates. The ratio of the absorbances at 580 and 630 nm increased with the temperature increase in aqueous solution while no spectral changes were observed in THF (Figure S1). Our data shows that aggregation of compound **1** leads to fluorescence quenching of both $S_1 \rightarrow S_0$ and $S_2 \rightarrow S_0$ transitions (a faint and broad band was recorded between 600 and 750 nm, alongside a weak band at 515 nm). The addition of bovine serum albumin (BSA) while exciting at 560 nm led to an emission band centered at 590 nm ($S_1 \rightarrow S_0$ transition), suggesting a shift in the equilibrium toward the non-aggregated form of **1** (Figure 4b). Exciting at 465 nm, the intensity of both the band centered at 530 nm ($S_2 \rightarrow S_0$ transition) and the tail extending beyond 575 nm ($S_2/S_1 \rightarrow S_0$ transition) also increases upon addition of BSA. Interestingly, the fluorescence intensity associated with the $S_2/S_1 \rightarrow S_0$ process shows a higher increase than the fluorescence intensity from the $S_2 \rightarrow S_0$ transition, as evident in the normalized emission spectrum (Figure S5). BSA is frequently used as a model to test new fluorophores as probes for protein surface hydrophobicity.[37] That protein contains two hydrophobic pockets (binding sites I and II)[38] along with diverse superficial hydrophobic areas.[37] The non-aggregated form of **1** (emissive) could be stabilized in the hydrophobic regions of the protein recovering the fluorescence emission. In accordance with this hypothesis, the fluorescence enhancement is reversed by adding a specific site I binder as warfarin, showing that **1** is displaced from the site I and the equilibrium is shifted toward the aggregated form of **1** (non-emissive) (Figure 4c).[39] Nevertheless, the fluorescence emission is not fully quenched when the concentration of warfarin (1.25 mM) becomes 25-times higher than of **1** (50 µM) and hence the fluorophore can have more than one binding site. An increase in the fluorescence intensity akin to BSA was not observed in the presence of the pepsin, in accordance with a previous report of He et al.[40] who shown that BSA has higher affinity for hydrophobic phenolic compounds as gallotannins than pepsin. In this sense, pepsin has multiple binding sites for a hydrophilic antioxidant as glutathione in contrast with the single binding site found a hydrophobic antioxidant as melatonin.[41]

Compound **1** did not showed sensitivity to coconut oil or macromolecules such as DNA and Ficoll 40 (Figure S6) but is sensitive to the formation of BSA aggregates induced by heating and addition of NaCl to the protein solution.[42,43] The fluorescence intensity of the two emission bands of **1** increased with the incubation time of the protein at 80ºC (Figure 4d). The misfolding of BSA leads to exposure of hydrophobic amino acid residues to the surface of the protein and the aggregation of the protein.[44,45] As previously mentioned, protein misfolding and aggregation are physiological process associated with oxidative stress and is linked to various diseases.[11,13,14] Congo red, Nile red, and Thioflavine T are dyes commonly used for staining protein aggregates, particularly used for monitoring amyloid fibril assembly.[46–49] The potential use of compound **1** as a fluorescent probe for detecting protein misfolding and aggregation induced by oxidative stress is discussed below.

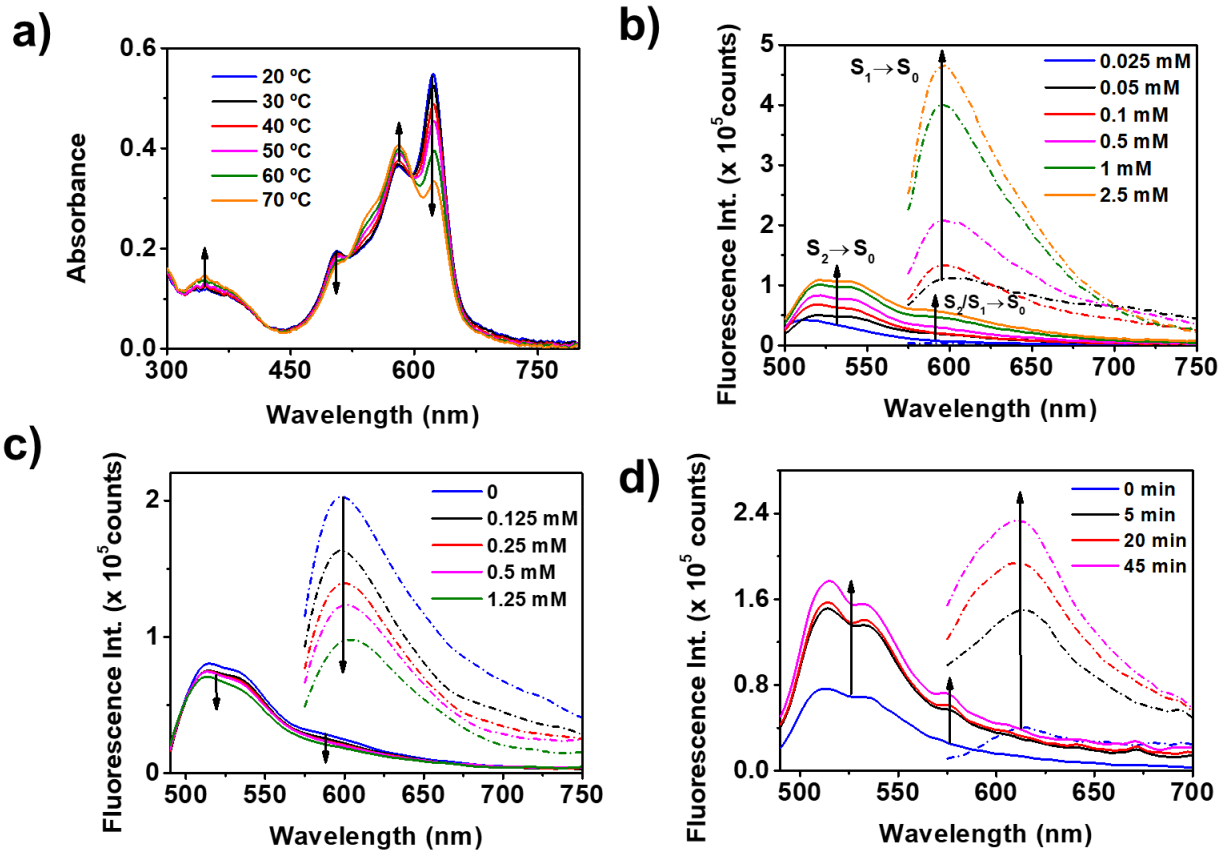


**Figure 4.** (a) Absorption spectrum of **1** (70 µM) at different temperatures in aqueous solution (b) Fluorescence emission spectra of **1** (50 µM) in presence of increasing concentrations of BSA ($\lambda_{ex}$ was 465 nm for solid lines and 560 nm for dashed lines). (c) Fluorescence emission spectra of **1** (50 µM) in presence of BSA (0.25 mM) and increasing concentrations of warfarin ($\lambda_{ex}$ was 465 nm for solid lines and 560 nm for dashed lines). (d) Fluorescence emission spectra of **1** (50 µM) in presence of BSA (250 µM), NaCl (125 mM) and different incubation times at 80 °C ($\lambda_{ex}$ was 465 nm for solid lines and 560 nm for dashed lines).

Different examples of fluorescent probes for hydrophobic proteins[37,50,51] and protein aggregation[52,53] have been reported recently. Some of them are based in BODIPY derivates[37,53] as compound **1**. The applications of these probes are mainly based on measurements of fluorescence intensity. It is known that fluorescence-lifetime probes have significant advantages over fluorescence-intensity probes because the fluorescence lifetime is not sensitive to either the fluorophore concentration, excitation source intensity or duration of light exposure.[54–56] Therefore, we are also interested in knowing if compound **1** could be also used as fluorescence-lifetime probe for hydrophobic proteins and protein aggregation. For that, the effect of BSA on the fluorescence decay profile of the unusual $S_2/S_1 \rightarrow S_0$ photophysical process was studied using FLIM (Figure 5a). This specific transition was chosen for two reasons: (i) its fluorescence intensity is very sensitive to albumin; (ii) the fluorescence background effects are minimized due to the large difference between the excitation wavelength (511 nm) and the acquired wavelengths (655 – 725 nm region). As showed in Figure 5b, the average fluorescence lifetime of the $S_2/S_1 \rightarrow S_0$ transition increased from 3.4 ns to 3.6 – 4.0 ns in presence of BSA (0.05 – 0.25 mM) while the opposite effect was observed in presence of other macromolecules as Ficoll 40 and coconut oil. The average fluorescence lifetime of **1** also increased in presence of BSA when the aggregation of the protein was induced by heating (80ºC) and adding NaCl.[57,58] Figure 5c shows how the fluorescence lifetime of the probe increases with the denaturation time of BSA. The fluorescence lifetimes of **1** reached approximately 5.0 ns after an incubation period of 45 minutes with BSA under heating. Figure 5d shows a FLIM image of BSA aggregates of tenths of micrometer in aqueous solution using compound **1** as probe. In contrast, no fluorescent aggregates are observed in absence of BSA or presence of non-denatured BSA (Figure 5d).

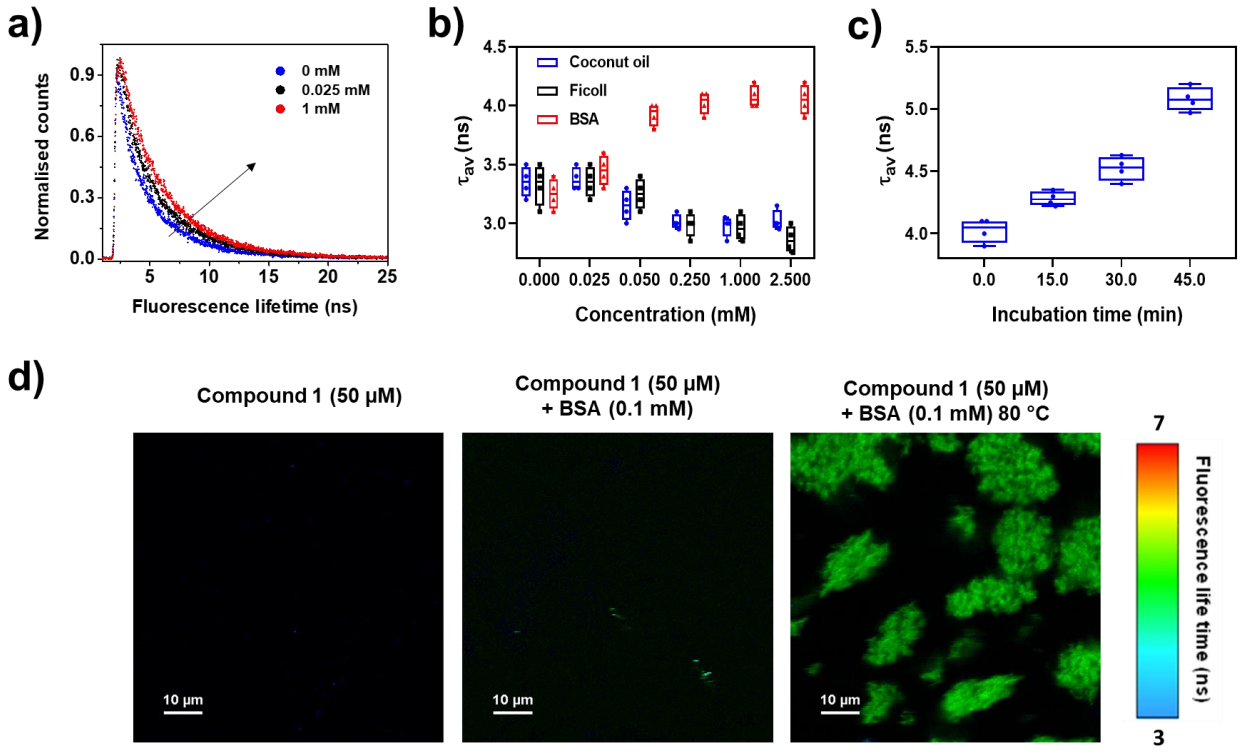


**Figure 5.** Fluorescence decay profiles, average fluorescence lifetimes and FLIM images acquired for compound **1** (50 μM in aqueous solution) in different experimental conditions ($\lambda_{ex}$ = 511 nm and a 690/70 nm bandpass filter for the fluorescence emission were used in all the experiments): (a) Fluorescence decay profile recorded for **1** adding increasing concentrations of BSA. (b) Average fluorescence lifetime determined for **1** adding increasing concentrations of coconut oil, Ficoll 40 and BSA. (c) Average fluorescence lifetime determined for **1** in aqueous solution with BSA (0.1 mM), NaCl (125 mM) and different incubation times at 80°C. (d) FLIM images of compound **1** (50 μM) in absence of BSA (left image) and presence of BSA (0.1 mM) (central image). The right image corresponds to BSA aggregates formed by heating (80°C, 45 minutes), adding NaCl (0.1 mM), and using compound **1** (50 μM) as fluorescent probe.

**Fluorescence Imaging in Live Cells.** The potential use of compound **1** as a fluorescent probe for detecting protein misfolding and aggregation was tested on two cancer cell lines (human breast cancer MCF-7 cells and human lung cancer A549 cells) under oxidative stress conditions. Fluorescence imaging experiments were carried out using two fluorescence microscopy approaches: one based on time-resolved fluorescence measurements (FLIM), and another based on fluorescence intensity measurements (two-photon fluorescence microscopy). FLIM experiments showed that compound **1** is efficiently taken up by MCF-7 cells (Figure 6). Cell viability remained high, above 93% for concentrations up to 0.5 mM after 24-hour incubation with **1** (Figure S6). In a similar way, a moderate impact on cell viability was reported for the homologous 7-azaindole-BODIPY derivative **3** after 48 hours of incubation in lymphoblast cells (K562 cell line, cell viability of about 70%).[10] The average fluorescence lifetime of compound **1** in MCF-7 cells treated was about 2.8 ns for incubation periods of

0.5 and 1 hour. There was a slight increase to 3.4 ns after 3 hours of incubation (see control cells in Figures 6a, 6 and S8). Oxidative stress was induced in MCF-7 cells by adding ethanol (1 M),[59] hydrogen peroxide (0.5 mM),[16–18] or cisplatin (10 μM).[60,61] Significant increases in the fluorescence lifetime were observed for a large fraction of cells, particularly for those exposed to hydrogen peroxide and cisplatin, following incubation periods of 1 and 3 hours (see Figures 6, 7 and S9-S11). Although a broad distribution of fluorescence lifetimes was observed for these cells, a significant proportion of the cells showed lifetimes within the range of 3 - 6 ns. Consequently, FLIM images showed regions with longer fluorescence lifetimes for cells treated with hydrogen peroxide and cisplatin (colored in green and red in Figure 6), contrasting to the shorter fluorescence lifetimes found in control cells (colored in blue). Considering the photophysical behavior of compound **1**, the regions with a longer lifetime in the vicinity of the nucleus were attributed to the accumulation of misfolded proteins or aggregates. Regarding cisplatin, our results are consistent with previous studies. For instance, the formation of protein aggregates and the increase of reactive oxygen species are concomitant processes observed in kidney tubular cells after cisplatin administration.[62,63] The endoplasmic reticulum stress and unfolded protein aggregation also seems to be related to the cardiotoxicity of cisplatin in mice.[64]

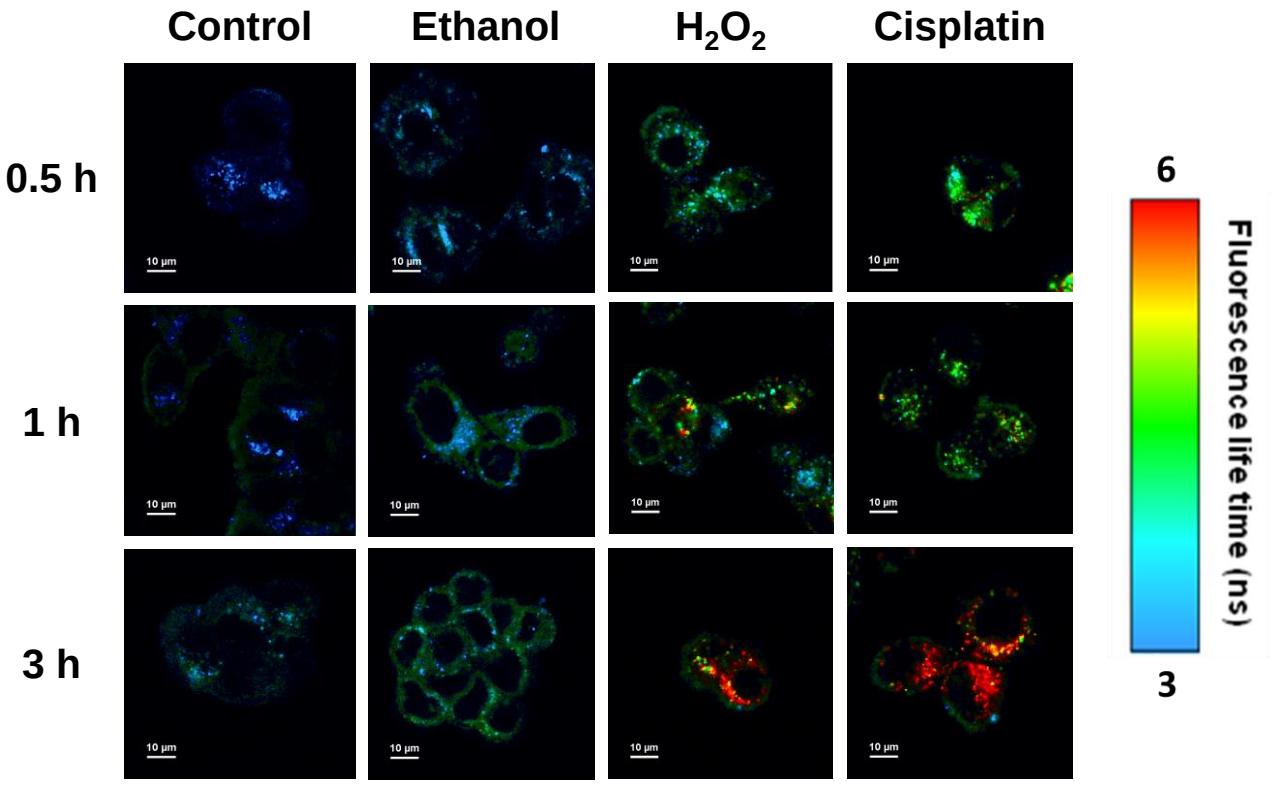

**Figure 6.** FLIM images acquired for MCF-7 cells treated with compound **1** (0.1 μM; $\lambda_{ex}$ = 511 nm; a 690/70 nm bandpass filter was used to collect the fluorescence emission). Additionally, MCF-7 cells were incubated with ethanol (1 M), hydrogen peroxide (0.5 mM) and cisplatin (10 μM) at different times (0.5, 1 and 3 hours).

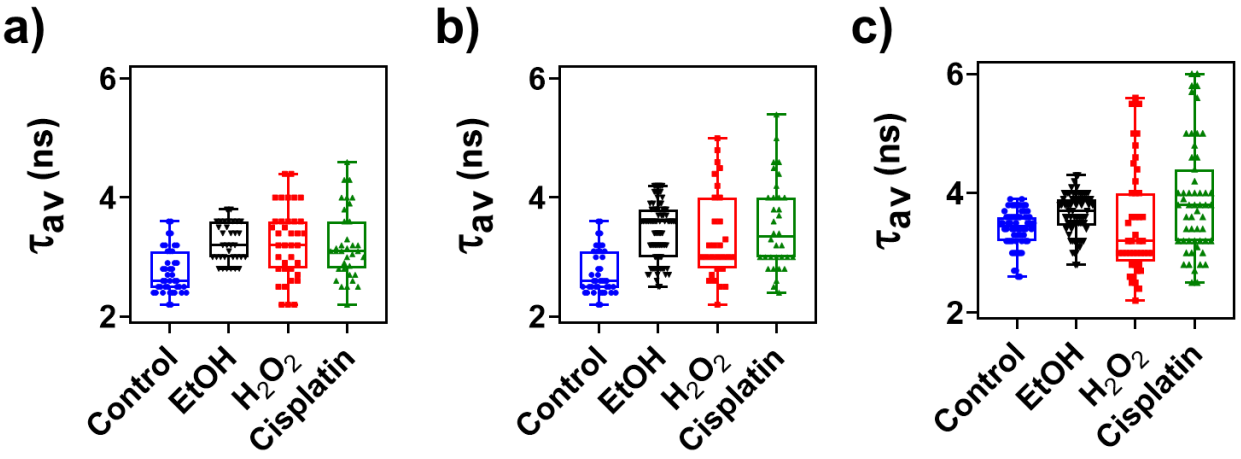


**Figure 7.** Box distribution plot of average fluorescence lifetimes ($\tau_{av}$) determined for MCF-7 cells treated with **1** (0.1 μM) along with ethanol (1 M), hydrogen peroxide (0.5 mM), (d) cisplatin (10 μM). The incubation time was (a) 0.5 hours, (b) 1 hour, (c) 3 hours.

The sensitivity of compound **1** to protein misfolding and aggregation associated with oxidative stress was also evaluated in A549 cells using a two-photon fluorescence microscope. An excitation wavelength of 1022 nm was chosen in order to reach the $S_2$ state of compound **1** and the fluorescence emission was recorded in wavelength windows: 515 - 575 nm (green channel) and 650 - 750 nm (red channel) to monitor the florescence emission associate with the $S_2 \rightarrow S_0$ and $S_2/S_1 \rightarrow S_0$ transitions, respectively. Two-photon fluorescence microscopy images showed that compound **1** is efficiently taken up by control A549 cells (Figures 8a and S12). For the untreated cells, the fluorescence emission recorded in the green channel is more intense compared to that in the red channel. This scenario is modified in cells treated with ethanol, where the fluorescence intensity from the red channel significantly increases with respect to the green channel (Figures 8b, 8c and S12). The fluorescence emission collected in the red channel also increases with the incubation time. Again, the notable increase of fluorescence intensity associated to the $S_2/S_1 \rightarrow S_0$ transition (red channel) seems to be related to protein misfolding and aggregation induced by oxidative stress. These results are accordance with the findings of Kim et al., who showed that metabolic stress induces the formation of protein aggregates in A549 cells.[65] Additionally, two-photon fluorescence microscopy allows a deeper

penetration of the excitation laser beam into tissues and cell spheroids. Figure 9 shows that compound **1** can be taken up by cells in spheroids. After an incubation period of 24-hours, compound **1** stains the periphery of A549 cell spheroids and penetrates about 50 micrometers inside. These results open the door to the future use of compound **1** as fluorescent probe in more complex systems as tissues and even *in vivo* models.

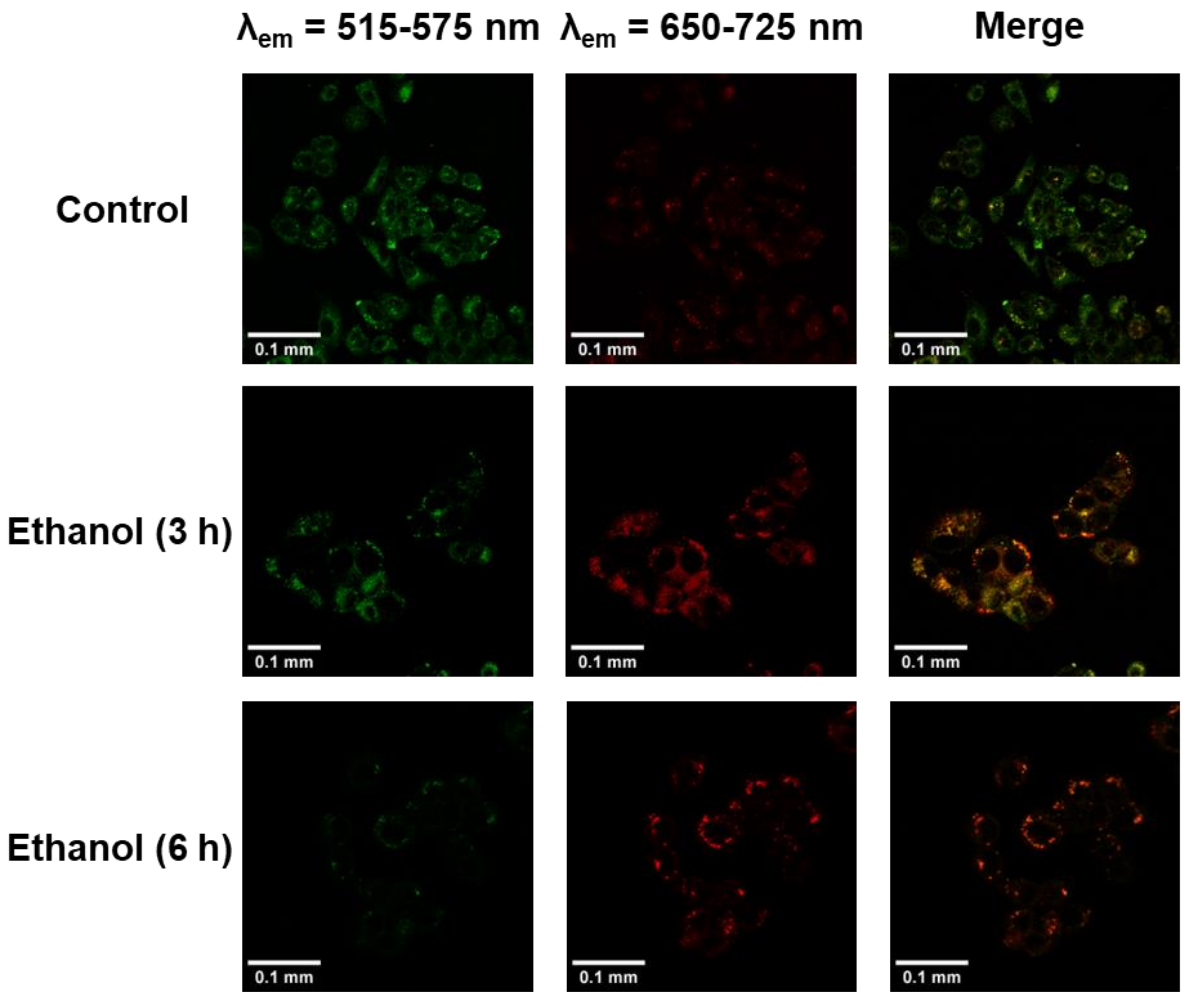


**Figure 8.** Two-photon fluorescence microscopy images recorded for A549 cells treated with compound **1** (0.1 μM) and ethanol (1 M) at different times (3 and 6 hours). Cell were excited at 1022 nm and the emission was collected in two wavelength windows: 515 - 575 nm (detector 1, green channel) and 650 - 750 nm (detector 2, red channel).

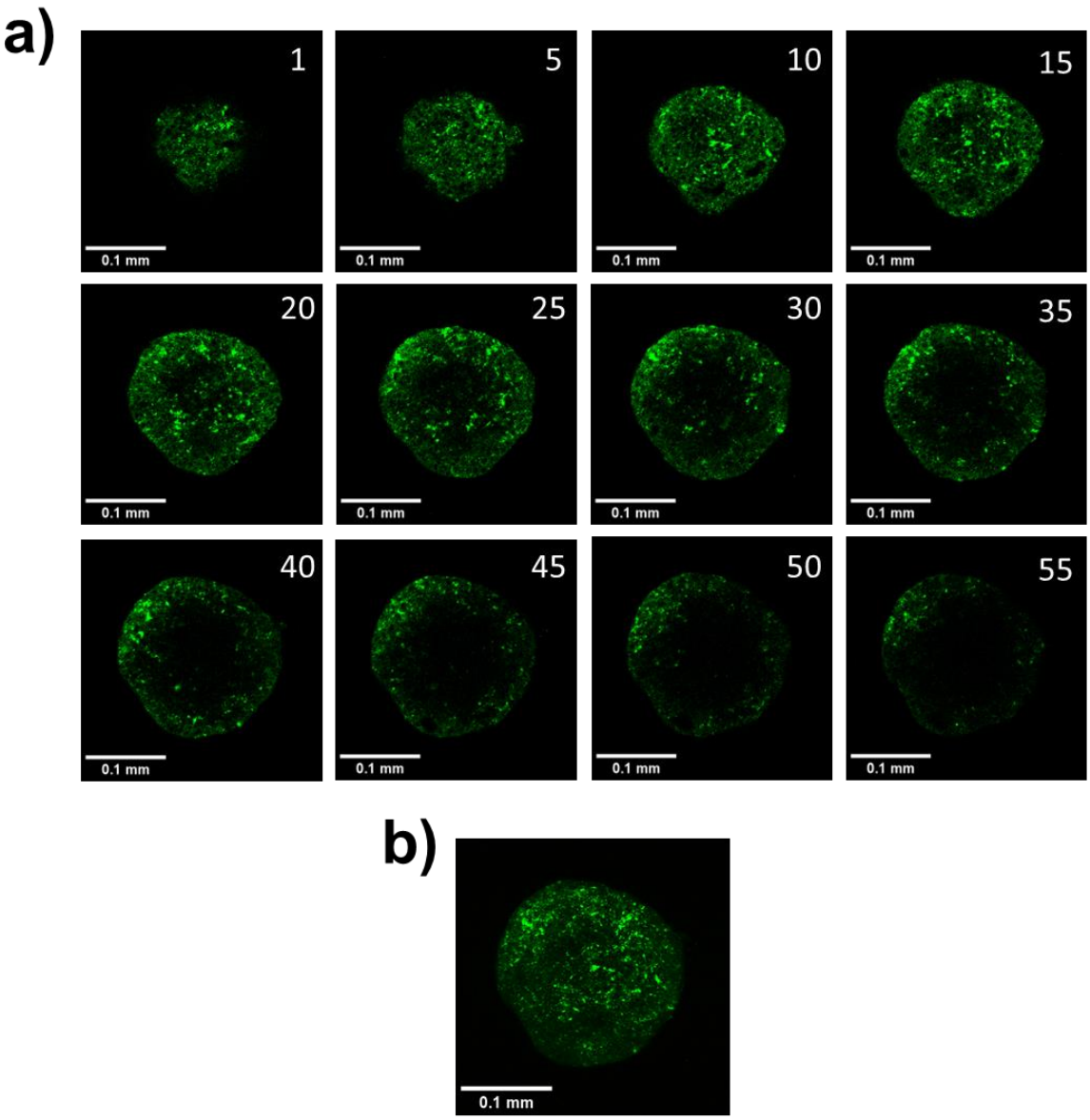


**Figure 9.** Two-photon fluorescence microscopy images of a A549 cell spheroid incubated with compound **1** (0.1 μM) for 24 hours ($\lambda_{ex}$ = 1022 nm; $\lambda_{em}$ = 550 - 725 nm). (a) Planes of A549 cell spheroids. Space between planes was 1 μm. (b) Z-projection of previous A549 cell spheroids planes.

**Synchrotron FTIR Microspectroscopy.** FTIR spectra of MCF-7 cells were recorded to provide additional information on the sensitivity of compound **1** to protein misfolding events. These spectra can inform about the protein structural changes in the cells under oxidative stress conditions. Average FTIR spectra of MCF-7 cells untreated and treated with cisplatin (10 μM for 3 hours) were acquired using a synchrotron light source. Figure 10a shows the average FTIR spectra of amide I and II regions for control and treated cells. Amide I band is shifted toward higher wavenumbers in the treated cells (1654 $cm^{-1}$) with respect to the control cells (1653 $cm^{-1}$). In contrast, amide II band is shifted toward lower wavenumbers (from 1541 $cm^{-1}$ for control cells to 1539 $cm^{-1}$ to treated cells). The shifts of the

amide I and II bands are typically associated with changes in secondary structure during misfolding and aggregation events.[66–70] The second derivate of the average FTIR spectra shows a minimum at 1655 $cm^{-1}$ and a shoulder at 1635 $cm^{-1}$ typically attributed to α-helix and β-sheet structures, respectively (Figure 10b).[66–70] As shown in Figure 10c, a decrease in the β-sheet/α-helix ratio (ratio of absorbances at 1635 and 1655 $cm^{-1}$) was observed in cells treated with cisplatin with respect to control cells. Maps of β-sheet/α-helix ratio acquired for groups of control and treated cells are shown in Figures 10d and 10e, respectively. The blue color is predominant in Figure 10e indicating the decrease of the β-sheet/α-helix ratio with respect the control cells (in green and yellow colors). The protein structural changes observed in MCF-7 cells under oxidative stress conditions are consistent with previous studies. For instance, an increase in α-helix structure was observed in gastric adenocarcinoma AGS cells treated with a brominated derivative of coelenteramine which has anticancer activity.[66] Altered protein α-helix structures were also detected in human embryonic liver WRL68 cells treated with doxorubicin.[69] Here, we have found that cisplatin, in similar conditions to the previous FLIM experiments, induce conformational changes in the proteins of MCF-7 cells. The observation of these changes is additional evidence of the sensitivity of compound **1** to protein misfolding and aggregation events associated with cellular stress responses.

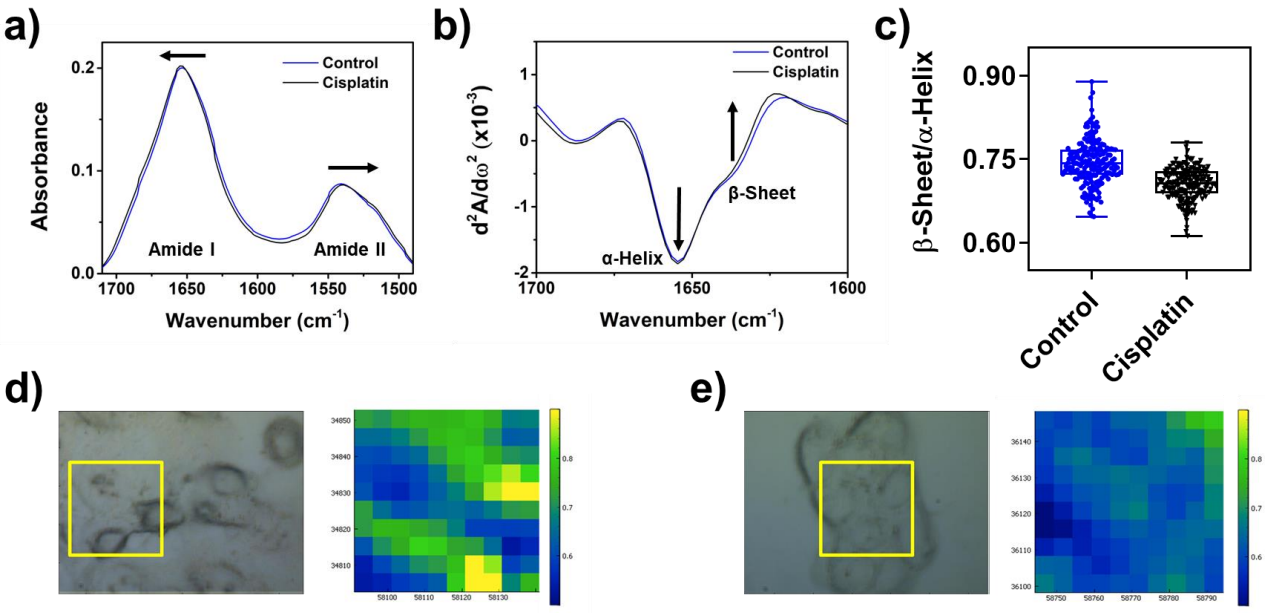


**Figure 10**. Average FTIR spectra of MCF-7 control cells and cells treated with cisplatin (10 µM; 3 hours) (N = 193 and 194, respectively). (a) Average FTIR spectra in the region between 1700 and 1500 $cm^{-1}$ (amide I and II bands). (b) Second derivate of the average FTIR spectra in the region between 1700 and 1600 $cm^{-1}$ (amide I band). (c) β-sheet/α-helix ratio

(ratio of absorbance at 1635 and 1655 $cm^{-1}$). (d,e) Bright field (left images) and β-sheet/α-helix ratio maps (right images) for a group of (d) control and (e) cisplatin-treated cells. The yellow squares indicate the scanned regions.

## CONCLUSIONS

The photophysical properties and sensing applications of a novel 7-azaindole-BODYPY derivative **1** have been studied here. Two emissive excited states ($S_1$ and $S_2$) were found for **1**, as well as an efficient IC process between both states. In aqueous solution, the fluorescence emission intensity of **1** is strongly quenched because of the formation of molecular aggregates. The fluorescence emission of **1** significantly increases upon the addition of albumin and formation of protein aggregates because the monomeric form of **1** is stabilized in the hydrophobic environments. Compound **1** showed less sensitivity to other macromolecules such as pepsin, DNA and Ficoll 40 as well as coconut oil. The fluorescence lifetime of **1** (particularly that coming from the transition $S_2/S_1 \rightarrow S_0$ which involves the internal conversion between $S_2$ and $S_1$ states) is highly sensitive to the presence of protein aggregates.

Different microscopy techniques, in two different cell lines, demonstrated that the $S_2/S_1 \rightarrow S_0$ transition of compound **1** can be used to monitor protein misfolding and aggregation associated with cellular stress responses. Firstly, FLIM images showed subcellular regions where the fluorescence lifetime significantly increased in breast cancer MCF-7 cells treated with ethanol, hydrogen peroxide and cisplatin. These regions were attributed to the accumulation of misfolded proteins or aggregates in response to the oxidative stress. Synchrotron FTIR microscopy showed that cisplatin induces conformational changes in the proteins of MCF-7 cells at short incubation periods (3 h) evidencing the sensitivity **1** to protein misfolding events associated with cellular stress responses. Secondly, two-photon fluorescence images showed that the emission intensity associated to the $S_2/S_1 \rightarrow S_0$ transition markedly increased when stress was induced in lung cancer A549 cells by adding ethanol. Compound **1** was also efficiently taken up and distributed by spheroids of A549 cells. These results encourage further research on the applications of **1** as fluorescent probe in more complex systems as tissues and even *in vivo* models.

**Acknowledgments**

This work is supported by 'Universidad de Castilla-La Mancha' through Projects 2022-GRIN-34143 and 2019-GRIN-27175, by KU Leuven (C14/22/085, IDN/20/021, and KA/20/026), and by the 'Junta de Comunidades de Castilla-La Mancha' by the grants SBPLY/21/180501/000050, SBPLY/23/180502/000013 and SBPLY/21/180501/000042. The authors also acknowledge support by the grants CPP2021-008597, and PID2021-128761OA-C22 and PID2020-117788RB-I00 funded by MCIN and Next Generation EU through Plan de Recuperación, Transformación y Resiliencia. P.C. and S.R. acknowledge financial support from the SuperCol project that received funding from the European Union's Horizon 2020 research and innovation program under the Marie Skłodowska-Curie grant agreement No. 860914. D.H. also thanks the 'Universidad de Castilla-La Mancha' for his predoctoral fellowship (2019/5964). The computational study was performed in SSC (Servicio de Supercomputación) from Universidad de Castilla-La Mancha. The authors thank ALBA Synchrotron Facility for beamtime allocation proposal number 2023027543 (instrument BL01 - MIRAS).

## ASSOCIATED CONTENT

**Supporting Information.** Additional details on synthesis. Additional information on spectroscopic characterization (Figures S1-S6). DFT calculations. Figure of cytotoxicity assays (Figure S7). Additional FLIM images (Figures S8-S11) and two-photon fluorescence microscopy images (Figure S12).

## AUTHOR INFORMATION

### Corresponding Authors

* **Andrés Garzón-Ruiz** – University of Castilla-La Mancha, Faculty of Pharmacy, Albacete, Spain; orcid.org/0000-0002-0077-4562; Email: andres.garzon@uclm.es

* **Eva M. García Frutos** – Instituto de Ciencia de Materiales de Madrid (ICMM), CSIC, Madrid, Spain; orcid.org/0000-0001-6270-1126; Email: emgfrutos@icmm.csic.es

* Susana Rocha – Molecular Imaging and Photonics, Department of Chemistry, KU Leuven, Leuven, Belgium; orcid.org/0000-0003-1258-9396; Email: susana.rocha@kuleuven.be

## Other Authors

**Diego Herrera Ochoa** – University of Castilla-La Mancha, Facultad de Farmacia, Albacete, Spain; orcid.org/0000-0002-3870-4113

**Iván Llano** – Instituto de Ciencia de Materiales de Madrid (ICMM), CSIC, Madrid, Spain.

**Consuelo Ripoll** – University of Castilla-La Mancha, Facultad de Farmacia, Albacete, Spain; orcid.org/0000-0002-9546-8735

**Pierre Cybulski** – Molecular Imaging and Photonics, Department of Chemistry, KU Leuven, Leuven, Belgium; orcid.org/0000-0002-2779-0677

**Martin Kreuzer** – ALBA Synchrotron Light Source, Cerdanyola Del Vallès, Barcelona, Spain; orcid.org/0000-0002-7305-5016

**Iván Bravo** – University of Castilla-La Mancha, Facultad de Farmacia and Centro Regional de Investigaciones Biomédicas (CRIB), Albacete, Spain; orcid.org/0000-0003-1589-5399

## Author Contributions

A.G.R., I.B. E.M.G.F. conceived the idea. A.G.R., I.B., E.M.G.F., S.R., and M.K. designed and supervised the experiments. D.H.O. performed measurements. I.L. carried out the synthesis of the studied compound. All authors contributed to the results discussions and agreed with the results. All authors contributed to writing the manuscript.

## Notes

The authors declare no competing financial interest.

## REFERENCES


(1) Ozcan, E.; Kazan, H. H.; Çoşut, B. Recent Chemo-/Biosensor and Bioimaging Studies Based on Indole-Decorated BODIPYs. *Luminescence*. John Wiley and Sons Ltd March 1, 2020, pp 168–177. https://doi.org/10.1002/bio.3719.

(2) Boens, N.; Leen, V.; Dehaen, W. Fluorescent Indicators Based on BODIPY. *Chem Soc Rev* **2012**, *41* (3), 1130–1172. https://doi.org/10.1039/c1cs15132k.

(3) Kowada, T.; Maeda, H.; Kikuchi, K. BODIPY-Based Probes for the Fluorescence Imaging of Biomolecules in Living Cells. *Chemical Society Reviews*. Royal Society of Chemistry July 21, 2015, pp 4953–4972. https://doi.org/10.1039/c5cs00030k.

(4) Jayasudha, P.; Manivannan, R.; Ciattini, S.; Chelazzi, L.; Elango, K. P. Selective Sensing of Cyanide in Aqueous Solution by Quinone-Indole Ensembles – Quantitative Effect of Substituents on the HBD Property of the Receptor Moiety. *Sens Actuators B Chem* **2017**, *242*, 736–745. https://doi.org/10.1016/j.snb.2016.11.117.

(5) Shao, J.; Wang, Y.; Lin, H.; Li, J.; Lin, H. A Novel Indole Phenylhydrazone Receptor: Synthesis and Recognition for Acetate Anion. *Sens Actuators B Chem* **2008**, *134* (2), 849–853. https://doi.org/10.1016/j.snb.2008.06.052.

(6) Rathikrishnan, K. R.; Indirapriyadharshini, V. K.; Ramakrishna, S.; Murugan, R. 4,7-Diaryl Indole-Based Fluorescent Chemosensor for Iodide Ions. *Tetrahedron* **2011**, *67* (22), 4025–4030. https://doi.org/10.1016/j.tet.2011.04.039.

(7) Manivannan, R.; Satheshkumar, A.; El-Mossalamy, E.-S. H.; Al-Harbi, L. M.; Kosa, S. A.; Elango, K. P. Design, Synthesis and Characterization of Indole Based Anion Sensing Receptors. *New J. Chem.* **2015**, *39* (5), 3936–3947. https://doi.org/10.1039/C4NJ01728E.

(8) Han, Y.; Dong, W.; Guo, Q.; Li, X.; Huang, L. The Importance of Indole and Azaindole Scaffold in the Development of Antitumor Agents. *European Journal of Medicinal Chemistry*. Elsevier Masson SAS October 1, 2020. https://doi.org/10.1016/j.ejmech.2020.112506.

(9) Mahapatra, A. K.; Maji, R.; Maiti, K.; Adhikari, S. S.; Das Mukhopadhyay, C.; Mandal, D. Ratiometric Sensing of Fluoride and Acetate Anions Based on a BODIPY-Azaindole Platform and Its Application to Living Cell Imaging. *Analyst* **2014**, *139* (1), 309–317. https://doi.org/10.1039/c3an01663c.

(10) Keşan, G.; Topaloğlu, B.; Özcan, E.; Kazan, H. H.; Eçik, E. T.; Şenkuytu, E.; Sengul, I. F.; Kandemir, H.; Çoşut, B. Azaindole-BODIPYs: Synthesis, Fluorescent Recognition of Hydrogen

Sulfate Anion and Biological Evaluation. *Spectrochim Acta A Mol Biomol Spectrosc* **2019**, *213*, 73–82. https://doi.org/10.1016/j.saa.2019.01.047.

(11) Alberti, S.; Hyman, A. A. Biomolecular Condensates at the Nexus of Cellular Stress, Protein Aggregation Disease and Ageing. *Nat Rev Mol Cell Biol* **2021**, *22* (3), 196–213. https://doi.org/10.1038/s41580-020-00326-6.

(12) Lévy, E.; El Banna, N.; Baïlle, D.; Heneman-Masurel, A.; Truchet, S.; Rezaei, H.; Huang, M. E.; Béringue, V.; Martin, D.; Vernis, L. Causative Links between Protein Aggregation and Oxidative Stress: A Review. *International Journal of Molecular Sciences*. MDPI AG August 2, 2019. https://doi.org/10.3390/ijms20163896.

(13) Mallucci, G. R.; Klenerman, D.; Rubinsztein, D. C. Developing Therapies for Neurodegenerative Disorders: Insights from Protein Aggregation and Cellular Stress Responses. *Annu Rev Cell Dev Biol* **2020**, *36* (1), 165–189. https://doi.org/10.1146/annurev-cellbio-040320-120625.

(14) Ross, C. A.; Poirier, M. A. Protein Aggregation and Neurodegenerative Disease. *Nat Med* **2004**, *10* (7), S10. https://doi.org/10.1038/nm1066.

(15) Van Zundert, I.; Maenhoudt, N.; De Vriendt, S.; Vankelecom, H.; Fortuni, B.; Rocha, S. Fluorescence Imaging of 3D Cell Models with Subcellular Resolution. *Bio Protoc* **2022**, *12* (14). https://doi.org/10.21769/BioProtoc.4469.

(16) Mahalingaiah, P. K. S.; Singh, K. P. Chronic Oxidative Stress Increases Growth and Tumorigenic Potential of MCF-7 Breast Cancer Cells. *PLoS One* **2014**, *9* (1). https://doi.org/10.1371/journal.pone.0087371.

(17) Ransy, C.; Vaz, C.; Lombès, A.; Bouillaud, F. Use of H2O2 to Cause Oxidative Stress, the Catalase Issue. *Int J Mol Sci* **2020**, *21* (23), 1–14. https://doi.org/10.3390/ijms21239149.

(18) Gille, J. J. P.; Joenje, H. *Cell Culture Models for Oxidative Stress: Superoxide and Hydrogen Peroxide versus Normobaric Hyperoxia*; 1992; Vol. 275.

(19) Ciftci, H.; Sever, B.; Bayrak, N.; Yıldız, M.; Yıldırım, H.; Tateishi, H.; Otsuka, M.; Fujita, M.; TuYuN, A. F. In Vitro Cytotoxicity Evaluation of Plastoquinone Analogues against Colorectal and Breast Cancers along with In Silico Insights. *Pharmaceuticals* **2022**, *15* (10). https://doi.org/10.3390/ph15101266.

(20) Ezzat, A.; Fayad, W.; Ibrahim, A.; Kamel, Z.; El-Diwany, A. I.; Shaker, K. H.; Esawy, M. A. Combination Treatment of MCF-7 Spheroids by Pseudomonas Aeruginosa HI1 Levan and Cisplatin. *Biocatal Agric Biotechnol* **2020**, *24*. https://doi.org/10.1016/j.bcab.2020.101526.

(21) Wawruszak, A.; Luszczki, J. J.; Grabarska, A.; Gumbarewicz, E.; Dmoszynska-Graniczka, M.; Polberg, K.; Stepulak, A. Assessment of Interactions between Cisplatin and Two Histone Deacetylase Inhibitors in MCF7, T47D and MDA-MB-231 Human Breast Cancer Cell Lines - An Isobolographic Analysis. *PLoS One* **2015**, *10* (11). https://doi.org/10.1371/journal.pone.0143013.

(22) Wawruszak, A.; Luszczki, J.; Halasa, M.; Okon, E.; Landor, S.; Sahlgren, C.; Rivero-Muller, A.; Stepulak, A. Sensitization of Mcf7 Cells with High Notch1 Activity by Cisplatin and Histone Deacetylase Inhibitors Applied Together. *Int J Mol Sci* **2021**, *22* (10). https://doi.org/10.3390/ijms22105184.

(23) Vrzal, R.; Štarha, P.; Dvořák, Z.; Trávníček, Z. Evaluation of in Vitro Cytotoxicity and Hepatotoxicity of Platinum(II) and Palladium(II) Oxalato Complexes with Adenine Derivatives as Carrier Ligands. *J Inorg Biochem* **2010**, *104* (10), 1130–1132. https://doi.org/10.1016/j.jinorgbio.2010.07.002.

(24) Yousef, I.; Ribó, L.; Crisol, A.; Šics, I.; Ellis, G.; Ducic, T.; Kreuzer, M.; Benseny-Cases, N.; Quispe, M.; Dumas, P.; Lefrançois, S.; Moreno, T.; García, G.; Ferrer, S.; Nicolas, J.; Aranda, M. A. G. MIRAS: The Infrared Synchrotron Radiation Beamline at ALBA. *Synchrotron Radiat News* **2017**, *30* (4), 4–6. https://doi.org/10.1080/08940886.2017.1338410.

(25) Toplak, M.; Birarda, G.; Read, S.; Sandt, C.; Rosendahl, S. M.; Vaccari, L.; Demšar, J.; Borondics, F. Infrared Orange: Connecting Hyperspectral Data with Machine Learning. *Synchrotron Radiat News* **2017**, *30* (4), 40–45. https://doi.org/10.1080/08940886.2017.1338424.

(26) Frisch, M. J.; Trucks, G. W.; Schlegel, H. B.; Scuseria, G. E.; Robb, M. A.; Cheeseman, J. R.; Scalmani, G.; Barone, V.; Petersson, G. A.; Nakatsuji, H.; Li, X.; Caricato, M.; Marenich, A. V.; Bloino, J.; Janesko, B. G.; Gomperts, R.; Mennucci, B.; Hratchian, H. P.; Ortiz, J. V.; Izmaylov, A. F.; Sonnenberg, J. L.; Williams-Young, D.; Ding, F.; Lipparini, F.; Egidi, F.; Goings, J.; Peng, B.; Petrone, A.; Henderson, T.; Ranasinghe, D.; Zakrzewski, V. G.; Gao, J.; Rega, N.; Zheng, G.; Liang, W.; Hada, M.; Ehara, M.; Toyota, K.; Fukuda, R.; Hasegawa, J.; Ishida, M.; Nakajima, T.; Honda, Y.; Kitao, O.; Nakai, H.; Vreven, T.; Throssell, K.; Montgomery, J. A.; Peralta, J. E.; Ogliaro, F.; Bearpark, M. J.; Heyd, J. J.; Brothers, E. N.; Kudin, K. N.; Staroverov, V. N.; Keith, T. A.; Kobayashi, R.; Normand, J.; Raghavachari, K.; Rendell, A. P.; Burant, J. C.; Iyengar, S. S.; Tomasi, J.; Cossi, M.; Millam, J. M.; Klene, M.; Adamo, C.; Cammi, R.; Ochterski, J. W.; Martin, R. L.; Morokuma, K.; Farkas, O.; Foresman, J. B.; Fox, D. J. Gaussian 16, Revision C.01. **2016**.

(27) Lee, C.; Yang, W.; Parr, R. G. PhysRevB.37.785. *Phys. Rev. B* **1988**, *37*, 785.

(28) Parr, Y. A.; Miehlich, B.; Savin, A.; Stoll, H.; Preuss, H. *RESULTS OBTAINED WITH THE CORRELATION ENERGY DENSITY FUNCTIONALS OF*; 1989; Vol. 157.

(29) Becke, A. D. Phys. Rev. A. *Phys. Rev. A* **1988**, *38*, 3098. https://doi.org/https://doi.org/10.1103/PhysRevA.38.3098.

(30) Cossi, M.; Rega, N.; Scalmani, G.; Barone, V. *Energies, Structures, and Electronic Properties of Molecules in Solution with the C-PCM Solvation Model*; 2003; Vol. 24.

(31) Tomasi, J.; Mennucci, B.; Cammi, R. Quantum Mechanical Continuum Solvation Models. *Chemical Reviews*. American Chemical Society 2005, pp 2999–3093. https://doi.org/10.1021/cr9904009.

(32) Momeni, M. R.; Brown, A. Why Do TD-DFT Excitation Energies of BODIPY/Aza-BODIPY Families Largely Deviate from Experiment? Answers from Electron Correlated and Multireference Methods. *J Chem Theory Comput* **2015**, *11* (6), 2619–2632. https://doi.org/10.1021/ct500775r.

(33) Alkhatib, Q.; Helal, W.; Marashdeh, A. Accurate Predictions of the Electronic Excited States of BODIPY Based Dye Sensitizers Using Spin-Component-Scaled Double-Hybrid Functionals: A TD-DFT Benchmark Study. *RSC Adv* **2022**, *12* (3), 1704–1717. https://doi.org/10.1039/d1ra08795a.

(34) Cho, D. W.; Fujitsuka, M.; Ryu, J. H.; Lee, M. H.; Kim, H. K.; Majima, T.; Im, C. S2 Emission from Chemically Modified BODIPYs. *Chemical Communications* **2012**, *48* (28), 3424–3426. https://doi.org/10.1039/c2cc30569k.

(35) Schäfer, C.; Mony, J.; Olsson, T.; Börjesson, K. Entropic Mixing Allows Monomeric-Like Absorption in Neat BODIPY Films. *Chemistry - A European Journal* **2020**, *26* (63), 14295–14299. https://doi.org/10.1002/chem.202002463.

(36) Descalzo, A. B.; Ashokkumar, P.; Shen, Z.; Rurack, K. On the Aggregation Behaviour and Spectroscopic Properties of Alkylated and Annelated Boron-Dipyrromethene (BODIPY) Dyes in Aqueous Solution. *ChemPhotoChem* **2020**, *4* (2), 120–131. https://doi.org/10.1002/cptc.201900235.

(37) Dorh, N.; Zhu, S.; Dhungana, K. B.; Pati, R.; Luo, F. T.; Liu, H.; Tiwari, A. BODIPY-Based Fluorescent Probes for Sensing Protein Surface-Hydrophobicity. *Sci Rep* **2015**, *5*. https://doi.org/10.1038/srep18337.

(38) Ghuman, J.; Zunszain, P. A.; Petitpas, I.; Bhattacharya, A. A.; Otagiri, M.; Curry, S. Structural Basis of the Drug-Binding Specificity of Human Serum Albumin. *J Mol Biol* **2005**, *353* (1), 38–52. https://doi.org/10.1016/j.jmb.2005.07.075.

(39) Rabbani, G.; Ahn, S. N. Structure, Enzymatic Activities, Glycation and Therapeutic Potential of Human Serum Albumin: A Natural Cargo. *International Journal of Biological Macromolecules*. Elsevier B.V. February 15, 2019, pp 979–990. https://doi.org/10.1016/j.ijbiomac.2018.11.053.

(40) He, Q.; Shi, B.; Yao, K. Interactions of Gallotannins with Proteins, Amino Acids, Phospholipids and Sugars. *Food Chem* **2006**, *95* (2), 250–254. https://doi.org/10.1016/j.foodchem.2004.11.055.

(41) Li, X.; Ni, T. Binding of Glutathione and Melatonin to Pepsin Occurs via Different Binding Mechanisms. *European Biophysics Journal* **2016**, *45* (2), 165–174. https://doi.org/10.1007/s00249-015-1085-y.

(42) Park, J. H.; Jackman, J. A.; Ferhan, A. R.; Ma, G. J.; Yoon, B. K.; Cho, N. J. Temperature-Induced Denaturation of BSA Protein Molecules for Improved Surface Passivation Coatings. *ACS Appl Mater Interfaces* **2018**, *10* (38), 32047–32057. https://doi.org/10.1021/acsami.8b13749.

(43) Liu, X.; Zhang, W.; Liu, J.; Pearce, R.; Zhang, Y.; Zhang, K.; Ruan, Q.; Yu, Y.; Liu, B. Mg2+ Inhibits Heat-Induced Aggregation of BSA: The Mechanism and Its Binding Site. *Food Hydrocoll* **2020**, *101*. https://doi.org/10.1016/j.foodhyd.2019.105450.

(44) Lebedeva, N. S.; Yurina, E. S.; Gubarev, Y. A.; Koifman, O. I. Molecular Mechanisms Causing Albumin Aggregation. The Main Role of the Porphyrins of the Blood Group. *Spectrochim Acta A Mol Biomol Spectrosc* **2021**, *246*. https://doi.org/10.1016/j.saa.2020.118975.

(45) Wen, L.; Lyu, M.; Xiao, H.; Lan, H.; Zuo, Z.; Yin, Z. Protein Aggregation and Performance Optimization Based on Microconformational Changes of Aromatic Hydrophobic Regions. *Mol Pharm* **2018**, *15* (6), 2257–2267. https://doi.org/10.1021/acs.molpharmaceut.8b00115.

(46) Xue, C.; Lin, T. Y.; Chang, D.; Guo, Z. Thioflavin T as an Amyloid Dye: Fibril Quantification, Optimal Concentration and Effect on Aggregation. *R Soc Open Sci* **2017**, *4* (1). https://doi.org/10.1098/rsos.160696.

(47) Yakupova, E. I.; Bobyleva, L. G.; Vikhlyantsev, I. M.; Bobylev, A. G. Congo Red and Amyloids: History and Relationship. *Bioscience Reports*. Portland Press Ltd January 15, 2019. https://doi.org/10.1042/BSR20181415.

(48) Frid, P.; Anisimov, S. V.; Popovic, N. Congo Red and Protein Aggregation in Neurodegenerative Diseases. *Brain Research Reviews*. January 2007, pp 135–160. https://doi.org/10.1016/j.brainresrev.2006.08.001.

(49) Kundel, F.; Tosatto, L.; Whiten, D. R.; Wirthensohn, D. C.; Horrocks, M. H.; Klenerman, D. Shedding Light on Aberrant Interactions – a Review of Modern Tools for Studying Protein Aggregates. *FEBS Journal*. Blackwell Publishing Ltd October 1, 2018, pp 3604–3630. https://doi.org/10.1111/febs.14409.

(50) Peng, L.; Wei, R.; Li, K.; Zhou, Z.; Song, P.; Tong, A. A Ratiometric Fluorescent Probe for Hydrophobic Proteins in Aqueous Solution Based on Aggregation-Induced Emission. *Analyst* **2013**, *138* (7), 2068–2072. https://doi.org/10.1039/c3an36634k.

(51) Chen, Y.; Li, K.; Zhang, S.; Xu, P.; Song, B. Turn-on Fluorescence Probe for BSA Detection and Selective Cell Imaging. *Dyes and Pigments* **2022**, *202*. https://doi.org/10.1016/j.dyepig.2022.110267.

(52) Yang, S.; Liu, X.; Wang, S.; Song, J.; Wu, J.; Shen, B.; Jia, H.; Guo, S.; Wang, Y.; Yang, Y.; Jiang, Y.; Yang, H.; Chang, J. Chalcone Derivatives as Dual-Sensitive Fluorescent Probe for Protein Aggregation Investigation. *Sens Actuators B Chem* **2023**, *395*. https://doi.org/10.1016/j.snb.2023.134514.

(53) Mora, A. K.; Murudkar, S.; Shivran, N.; Mula, S.; Chattopadhyay, S.; Nath, S. Monitoring the Formation of Insulin Oligomers Using a NIR Emitting Glucose-Conjugated BODIPY Dye. *Int J Biol Macromol* **2021**, *166*, 1121–1130. https://doi.org/10.1016/j.ijbiomac.2020.10.267.

(54) Liu, C.; Wang, X.; Zhou, Y.; Liu, Y. Timing and Operating Mode Design for Time-Gated Fluorescence Lifetime Imaging Microscopy. *The Scientific World Journal* **2013**, *2013*. https://doi.org/10.1155/2013/801901.

(55) Berezin, M. Y.; Achilefu, S. Fluorescence Lifetime Measurements and Biological Imaging. *Chem Rev* **2010**, *110* (5), 2641–2684. https://doi.org/10.1021/cr900343z.

(56) Ruedas-Rama, M. J.; Alvarez-Pez, J. M.; Crovetto, L.; Paredes, J. M.; Orte, A. FLIM Strategies for Intracellular Sensing; 2014; pp 191–223. https://doi.org/10.1007/4243_2014_67.

(57) Park, J. H.; Jackman, J. A.; Ferhan, A. R.; Ma, G. J.; Yoon, B. K.; Cho, N. J. Temperature-Induced Denaturation of BSA Protein Molecules for Improved Surface Passivation Coatings. *ACS Appl Mater Interfaces* **2018**, *10* (38), 32047–32057. https://doi.org/10.1021/acsami.8b13749.

(58) Liu, X.; Zhang, W.; Liu, J.; Pearce, R.; Zhang, Y.; Zhang, K.; Ruan, Q.; Yu, Y.; Liu, B. Mg2+ Inhibits Heat-Induced Aggregation of BSA: The Mechanism and Its Binding Site. *Food Hydrocoll* **2020**, *101*. https://doi.org/10.1016/j.foodhyd.2019.105450.

(59) Comporti, M.; Signorini, C.; Leoncini, S.; Gardi, C.; Ciccoli, L.; Giardini, A.; Vecchio, D.; Arezzini, B. Ethanol-Induced Oxidative Stress: Basic Knowledge. *Genes and Nutrition*. June 2010, pp 101–109. https://doi.org/10.1007/s12263-009-0159-9.

(60) Yu, W.; Chen, Y.; Dubrulle, J.; Stossi, F.; Putluri, V.; Sreekumar, A.; Putluri, N.; Baluya, D.; Lai, S. Y.; Sandulache, V. C. Cisplatin Generates Oxidative Stress Which Is Accompanied by Rapid Shifts in Central Carbon Metabolism. *Sci Rep* **2018**, *8* (1). https://doi.org/10.1038/s41598-018-22640-y.

(61) Pratibha, R.; Sameer, R.; Rataboli, P. V.; Bhiwgade, D. A.; Dhume, C. Y. Enzymatic Studies of Cisplatin Induced Oxidative Stress in Hepatic Tissue of Rats. *Eur J Pharmacol* **2006**, *532* (3), 290–293. https://doi.org/10.1016/j.ejphar.2006.01.007.

(62) Takahashi, A.; Kimura, T.; Takabatake, Y.; Namba, T.; Kaimori, J.; Kitamura, H.; Matsui, I.; Niimura, F.; Matsusaka, T.; Fujita, N.; Yoshimori, T.; Isaka, Y.; Rakugi, H. Autophagy Guards against Cisplatin-Induced Acute Kidney Injury. *American Journal of Pathology* **2012**, *180* (2), 517–525. https://doi.org/10.1016/j.ajpath.2011.11.001.

(63) Sears, S. M.; Siskind, L. J. Potential Therapeutic Targets for Cisplatin-Induced Kidney Injury: Lessons from Other Models of AKI and Fibrosis. *Journal of the American Society of Nephrology*. American Society of Nephrology July 1, 2021, pp 1559–1567. https://doi.org/10.1681/ASN.2020101455.

(64) Ma, H.; Jones, K. R.; Guo, R.; Xu, P.; Shen, Y.; Ren, J. Cisplatin Compromises Myocardial Contractile Function and Mitochondrial Ultrastructure: Role of Endoplasmic Reticulum Stress. *Clin Exp Pharmacol Physiol* **2010**, *37* (4), 460–465. https://doi.org/10.1111/j.1440-1681.2009.05323.x.

(65) Kang. Role of Reactive Oxygen Species-Dependent Protein Aggregation in Metabolic Stress-Induced Necrosis. *Int J Oncol* **2010**, *37* (1). https://doi.org/10.3892/ijo_00000657.

(66) Magalhaes, C. M.; Dučić, T.; Pereira, R. B.; González-Berdullas, P.; Rodríguez-Borges, J. E.; Pereira, D. M.; Esteves da Silva, J. C. G.; Algarra, M.; Pinto da Silva, L. Synchrotron-Based FTIR Evaluation of Biochemical Changes in Cancer and Noncancer Cells Induced by Brominated Marine Coelenteramine. *Arch Biochem Biophys* **2023**, *743*. https://doi.org/10.1016/j.abb.2023.109660.

(67) Dučić, T.; Koch, J. C. Synchrotron-Based Fourier-Transform Infrared Micro-Spectroscopy of Cerebrospinal Fluid from Amyotrophic Lateral Sclerosis Patients Reveals a Unique Biomolecular Profile. *Cells* **2023**, *12* (11). https://doi.org/10.3390/cells12111451.

(68) Dróżdż, A.; Sławińska-Brych, A.; Kubera, D.; Kimsa-Dudek, M.; Gola, J. M.; Adamska, J.; Kruszniewska-Rajs, C.; Matwijczuk, A.; Karcz, D.; Dąbrowski, W.; Stepulak, A.; Gagoś, M. Effect of Antibiotic Amphotericin B Combinations with Selected 1,3,4-Thiadiazole Derivatives on RPTECs in an In Vitro Model. *Int J Mol Sci* **2022**, *23* (23). https://doi.org/10.3390/ijms232315260.

(69) Zhou, X.; Zhong, J.; Yu, W.; Tang, Y. Synchrotron Radiation-Based Fourier Transform Infrared Microspectroscopy Investigation of WRL68 Cells Treated with Doxorubicin. *Spectrochim Acta A Mol Biomol Spectrosc* **2022**, *283*. https://doi.org/10.1016/j.saa.2022.121773.

(70) Dučić, T.; Sanchez-Mata, A.; Castillo-Sanchez, J.; Algarra, M.; Gonzalez-Munoz, E. Monitoring Oocyte-Based Human Pluripotency Acquisition Using Synchrotron-Based FTIR Microspectroscopy Reveals Specific Biomolecular Trajectories. *Spectrochim Acta A Mol Biomol Spectrosc* **2023**, *297*. https://doi.org/10.1016/j.saa.2023.122713.